A Semi-Empirical Two Step Carbon Corrosion Reaction Model in PEM Fuel Cells

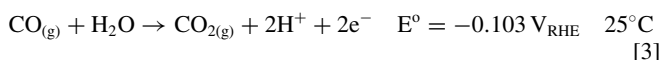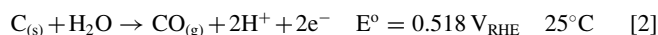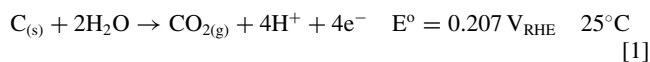A. P. Young,[*,z] V. Colbow, D. Harvey, E. Rogers, and S. Wessel

Ballard Power Systems, Burnaby, British Columbia V5J 5J8, Canada

The cathode CL of a polymer electrolyte membrane fuel cell (PEMFC) was exposed to high potentials, 1.0 to 1.4 V versus a reversible hydrogen electrode (RHE), that are typically encountered during start up/shut down operation. While both platinum dissolution and carbon corrosion occurred, the carbon corrosion effects were isolated and modeled. The presented model separates the carbon corrosion process into two reaction steps; (1) oxidation of the carbon surface to carbon-oxygen groups, and (2) further corrosion of the oxidized surface to carbon dioxide/monoxide. To oxidize and corrode the cathode catalyst carbon support, the CL was subjected to an accelerated stress test cycled the potential from 0.6 V_{RHE} to an upper potential limit (UPL) ranging from 0.9 to 1.4 V_{RHE} at varying dwell times. The reaction rate constants and specific capacitances of carbon and platinum were fitted by evaluating the double layer capacitance (Cdl) trends. Carbon surface oxidation increased the Cdl due to increased specific capacitance for carbon surfaces with carbon-oxygen groups, while the second corrosion reaction decreased the Cdl due to loss of the overall carbon surface area. The first oxidation step differed between carbon types, while both reaction rate constants were found to have a dependency on UPL, temperature, and gas relative humidity.
© 2013 The Electrochemical Society. [DOI: 10.1149/2.061304jes] All rights reserved.

Early polymer electrolyte membrane fuel cell (PEMFC) research used platinum black as the catalyst for both the cathode and anode electrodes. These electrodes were costly due to their very high Pt loadings ($>>1.0$ mg/cm^2). One of the ways of reducing the platinum loading was to replace platinum black with dispersed platinum nanoparticles on a carbon support. The smaller platinum particles on carbon enabled a reduced Pt loading of the cathode to less than 0.5 mg/cm^2, while maintaining the required platinum surface area required for high fuel cell performance. Although cost was reduced, the durability of the fuel cell was negatively impacted. At potentials greater than 0.2 V_{RHE} (reversible hydrogen electrode), the carbon support is thermodynamically unstable and able to oxidize to carbon dioxide (CO$_2$) and/or carbon monoxide (CO) [Eqs. 1–3],[1] leaving the platinum unsupported and inactive. Furthermore, due to the loss of support the platinum particles have been shown to agglomerate into larger particles, dissolve into the ionomer, or get washed out of the system.[2,3]

$$C_{(s)} + 2H_2O \rightarrow CO_{2(g)} + 4H^+ + 4e^- \quad E^o = 0.207\,V_{RHE} \quad 25°C \tag{1}$$

$$C_{(s)} + H_2O \rightarrow CO_{(g)} + 2H^+ + 2e^- \quad E^o = 0.518\,V_{RHE} \quad 25°C \tag{2}$$

$$CO_{(g)} + H_2O \rightarrow CO_{2(g)} + 2H^+ + 2e^- \quad E^o = -0.103\,V_{RHE} \quad 25°C \tag{3}$$

Even in the presence of platinum, the kinetics of carbon oxidation/corrosion is relatively slow; therefore, carbon is quite stable under normal PEMFC operating conditions. In practice, elevated cathode potentials of greater than 1.2 V_{RHE} are required to oxidize carbon at reaction rates high enough to cause significant structural degradation. Normal PEMFC operation occurs between 0–1.0 V_{RHE}; however, upon fuel starvation or gas switching conditions (start-up and shutdown operation due to infiltration of oxygen into the normally hydrogen filled anode compartment during fuel cell off conditions) the cathode potential can exceed 1.2 V_{RHE}.[4] At these potentials both water and carbon oxidation takes place as shown in Equations 1–4.

$$H_2O \rightarrow \tfrac{1}{2}O_2 + 2H^+ + 2e^- \quad E^o = 1.230\,V_{RHE} \quad 25°C \tag{4}$$

The carbon lost at electrode potentials greater than 1.0 V_{RHE} reduces the effective platinum surface area and weakens the catalyst layer (CL) structure. Once a significant amount of carbon is lost as CO$_2$ and/or CO, the CL structure collapses, eventually leaving mainly

a film type structure of unsupported platinum and Nafion ionomer. To study the effects of gas switching an accelerated stress test (AST) was performed cycling the cathode potential between 0.6 V_{RHE} to an upper potential limit (UPL) between 0.9 to 1.4 V_{RHE} in an air atmosphere. This AST results in a mixture of multiple degradation mechanisms that PEMFCs experience during start-up and shutdown protocols; platinum dissolution/agglomeration and carbon support corrosion.

Typically different ASTs have been used to isolate and study each catalyst degradation mechanism independently;[5] however, to do this one must test under conditions that differ significantly from normal start-up/shutdown conditions. For example, the most often used AST to study carbon corrosion tests in a nitrogen environment and holds the cathode potential constant as opposed to cycling. This study is aimed to resolve the carbon corrosion degradation rates, independent of the Pt dissolution rate, using a more realistic AST in combination with sophisticated data analysis as opposed to changing the test conditions.

The carbon corrosion process was modeled as two reaction steps;[6,7] carbon surface oxidation to intermediate carbon-oxygen groups [Eq. 5] and further corrosion to carbon dioxide [Eq. 6], assuming that Eq. 1 is the dominant reaction pathway.

$$C_{(s)} + H_2O \rightarrow C - O_{ad} + 2H^+ + 2e^- \tag{5}$$

$$C\text{-}O_{ad} + H_2O \rightarrow CO_{2(g)} + 2H^+ + 2e^- \tag{6}$$
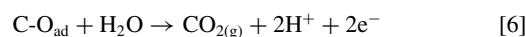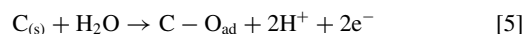
Throughout the remainder of this paper these two reaction steps will be referred to as the oxidation and corrosion reactions, respectively. The reaction rate constants are compared between two different carbons and their dependence on UPL, temperature, and gas relative humidity (RH) were investigated.

Cyclic voltammetry (CV) and electrochemical impedance spectroscopy (EIS) were used to measure the effective catalyst surface area (ECSA) and double layer capacitance (Cdl) throughout the AST to monitor the change of the platinum and carbon surface over time. Scanning electron microscopy (SEM) was used to measure changes in the cathode CL thickness and polarization analyzes were conducted to evaluate the performance loss associated with the AST. This communication focuses on the development of the semi-empirical model, and how this model can be used to predict performance loss as a function of UPL, temperature, and gas RH.

Experimental

Membrane electrode assembly (MEA) and test hardware.— The MEA used catalyst coated membrane (CCM) technology with a 0.4/0.1 mg/cm^2 (cathode/anode) platinum loading of a 50:50 Pt/C catalyst, on a DuPont Nafion NR211 membrane. Two different cathode catalysts were tested to compare differing corrosion resistance

*Electrochemical Society Active Member.
zE-mail: alan.young@ballard.com

Table I. Operating conditions for the standard fuel cell operation and the corrosion accelerated stress test.

Operating Conditions	Temp (°C)	Pressure (psig)	Oxidant Flow Rate (slpm)	Fuel Flow Rate (slpm)	Anode & Cathode Gas RH %	Current Density (A/cm^2)
Standard	75	5	9 (air)	4.45 (H$_2$)	100	1.3
AST	80	5	9 (air)	4.45 (H$_2$)	100	0

of the catalyst carbon support; a graphitic low surface area carbon (LSAC) support and a slightly less graphitic medium surface area carbon (MSAC) support.

The anode and cathode gas diffusion layers, consisting of a Ballard Material Products (BMP) carbon fiber paper with a carbon and Teflon sub-layer, were assembled with the CCM in a Kapton frame with a 45 cm^2 geometric area.

Testing was conducted in a state-of-the-art 1D bladder compression hardware with carbon composite plates utilizing a parallel flow field design for low pressure and uniform flow. High volume channels enabled the high flow rates (stoichiometry > 5) required to reduce temperature, pressure, and concentration gradients along the length of the cell to achieve the pseudo one-dimensional operating condition.

Operating conditions and degradation protocol.— The cell was conditioned at the standard steady state operating conditions of 75°C, 100%RH, 5 psig, 1.3 A/cm^2 as listed in Table I. The AST conditions (Table I) utilized 100% gas RH to maximize the amount of degradation[7,8] and minimize the required test duration. The voltage was cycled in an air (cathode)/H$_2$ (anode) environment from a lower potential limit of 0.6 V$_{RHE}$ for 30 s, to an UPL that varied between 0.9 to 1.4 V$_{RHE}$ for 60 s. During the AST period, CV and EIS measurements were conducted after 0, 50, 700, 1400, 2100, and 4700 cycles. SEM analysis was conducted with beginning of test (BOT) and degraded end of test (EOT) MEAs.

As discussed the standard AST held the UPL for 60 s in order to accelerate the degradation; however, in an operating system the PEMFC would only experience high UPLs for much shorter durations of less than 1 s. UPL dwell time testing between 5 and 600 s was conducted to evaluate the impact of dwell time at UPL on the corrosion rates. Testing dwell times less than 1 s could not be achieved due to equipment limitations.

Temperature and gas RH dependencies were also studied by varying the temperature between 60 to 90°C, and the reactants gas RH between 50 to 120%RH (where 120%RH signifies two phase flow). In these tests the dwell time was held at 600 s in order to reduce the platinum dissolution effects and increase the corrosion impacts, as will be discussed later.

The carbon loss was calculated by measuring the CO and CO$_2$ in the cathode and anode gas exhaust using a Fuji Electric ZRH IR CO and CO$_2$ gas analyzer.

CV.— CV scans were conducted using a Solartron SI1287 potentiostat to calculate the ECSA, the H$_2$ crossover current, and the Cdl. Hydrogen present at the anode acted as the reference electrode as the cathode potential was cycled between 0.1–1.2 V$_{RHE}$ at 20 mV/s. The ECSA was determined by CO stripping, assuming a charge density of 420 µC/cm^2 to break the linear Pt-CO bond.[9]

EIS.— EIS measurements were taken by applying a 10 mV AC perturbation signal with a 0.45 V$_{RHE}$ DC bias potential. A SI1287 Solartron potentiostat and a 1250 Solartron Hi Frequency Response analyzer were used in a 4-electrode configuration to sweep the frequency between 50 kHz to 0.05 Hz. The bias potential was applied to eliminate any pseudo-capacitive effects that result from hydrogen and oxygen adsorption-desorption.[10] Z-plot and Z-view software were used to conduct and analyze the EIS spectra to determine the impedance and capacitance. Measurements were taken in a nitrogen and hydrogen atmosphere on the cathode and anode, respectively. The EIS spectra were fit to an equivalent circuit representing a transmission line network of the porous CL. As discussed elsewhere[11] in greater detail, the fitted parameters consisted of the high frequency cell resistance, the cathode CL protonic resistance, and the Cdl.

Scanning electron microscopy.— After operation the MEAs were analyzed with a Philips XL30 SEM to detect changes in the MEA structure due to the carbon corrosion. MEA samples were cast into epoxy pucks. Pictures were taken using a backscatter detector at 400 x magnification and 15 kV. The membrane and CL thicknesses were measured. The cathode CL thickness, in conjunction with a carbon mass balance, was used to calculate the CL porosity in new and degraded samples.

Results and Discussion

Observations in ECSA.— The ECSA is plotted in Figures 1a and 2a for cathode CLs containing Pt catalyst supported on LSAC and MSAC, respectively. An increasing loss of ECSA with increasing
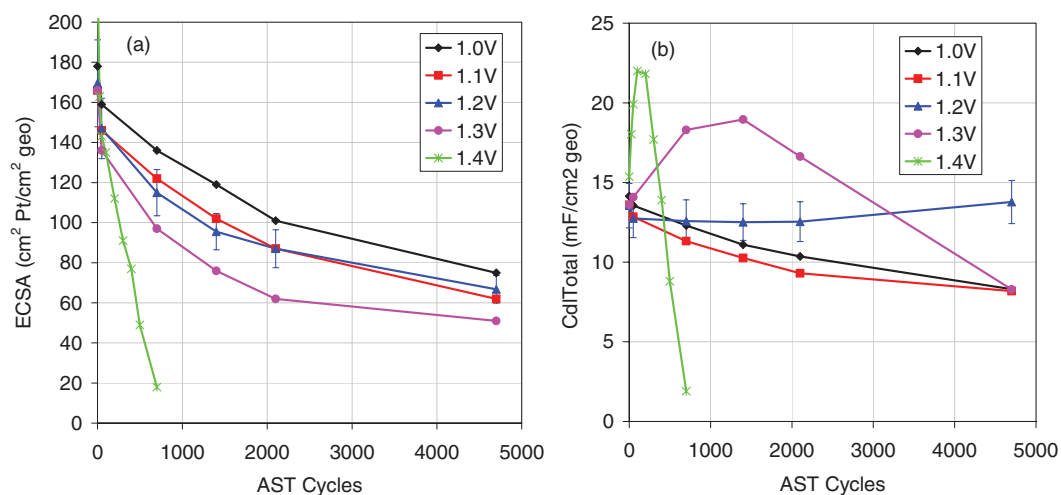

Figure 1. (a) the ECSA, and (b) the Cdl, as a function of AST cycles for the LSAC50 carbon support.
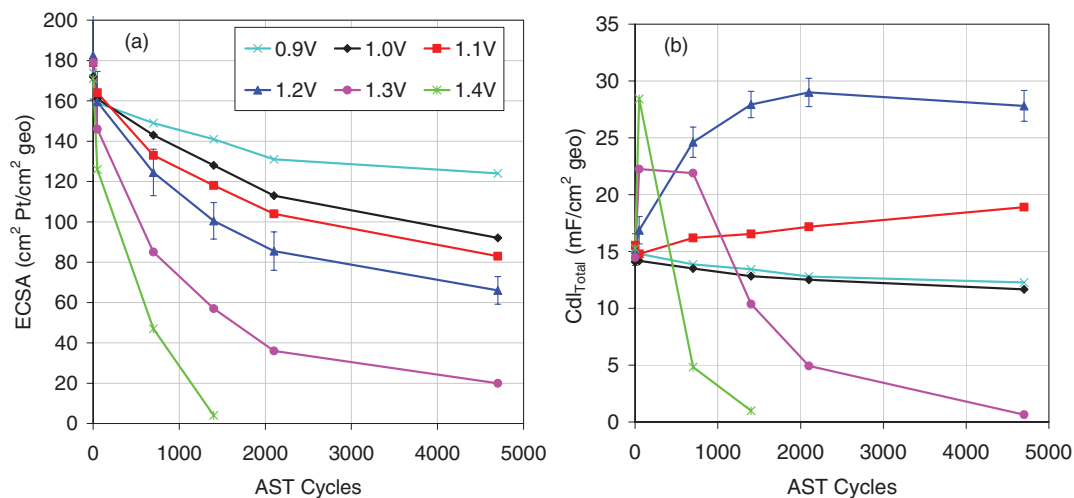
Figure 2. (a) the ECSA, and (b) the Cdl, as a function of AST cycles for the MSAC50 carbon support.

UPL is observed due to both increased carbon support oxidation and Pt dissolution/agglomeration.

The UPL dwell time study helped de-convolute the ECSA response between the carbon corrosion and Pt dissolution degradation mechanisms. Figure 3a shows the ECSA plotted against the total accumulated UPL time, which initially gives the impression that greater dwell times lead to less ECSA loss. Since the number of cycles is a known stressor for platinum dissolution[12] the lower ECSA loss at longer dwell times was associated with fewer AST cycles. Therefore, the ECSA was normalized by the cycle number, shown in Figure 3b, and resulted in greater platinum loss per cycle for longer dwell times.

This is consistent with accepted understanding; Matsumoto et al.[12] conducted analysis of both cycling and potential hold ASTs and showed a greater Pt dissolution rate with cycling, and an even greater dissolution rate by cycling in the presence of O_2 compared to N_2. The authors proposed that in the presence of O_2 there was a greater place exchange of oxygen into the Pt crystal resulting in high-order Pt oxide formation. Further, it is the cathodic reduction of higher-order Pt oxides which results in faster Pt dissolution compared to the commonly suspected anodic and/or chemical dissolution process that would be typical under a potential hold situation. Kongkanand et al.[13] found similar evidence through X-ray adsorption spectroscopy measurements. They also showed, via an electrochemical quartz crystal microbalance, that operation under O_2 or N_2 resulted in similar total oxide formation. Since the anodic driven oxide formation is similar, this provides further support that the cathodic driven dissolution of higher order Pt oxides is the cause of a faster Pt dissolution rate, and is the reason why there was greater Pt dissolution when cycling under air.

It is hypothesized that the greater platinum loss per cycle for longer dwell times seen here was due to the greater build up and place exchange of higher order Pt oxides that occurred during longer UPL dwell times. Reducing more oxide on the downward cycle caused greater de-stabilization of the platinum structure resulting in surface roughening and greater platinum dissolution. Although not shown, this trend also occurred when cycling to an upper potential of 1.0 V_{RHE}, where the impact of carbon corrosion was negligible.

X-ray diffraction and energy dispersive X-ray spectroscopy measurements obtained for all samples support the ECSA trends with an increase in the platinum crystallite size and platinum in the membrane due to the increased Pt dissolution and agglomeration.

Observations in Cdl.— The double layer capacitance was obtained from both CV and EIS measurements. Observed previously,[11] the CV and EIS Cdl measurements differed by a factor of 1 to 2. It is clarified here that the pseudo-capacitance part of the Pt oxide reduction peak
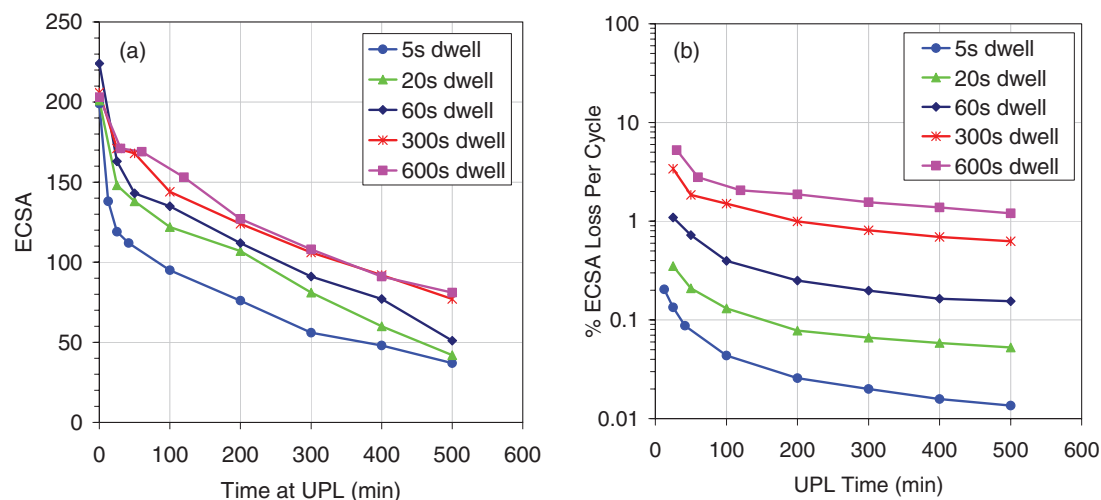

Figure 3. (a) the ECSA as a function of cumulative time at a 1.4 V UPL for different UPL dwell times, and (b) the % ECSA loss normalized by cycle number as a function of cycle dwell time and cumulative time at a 1.4 V UPL.
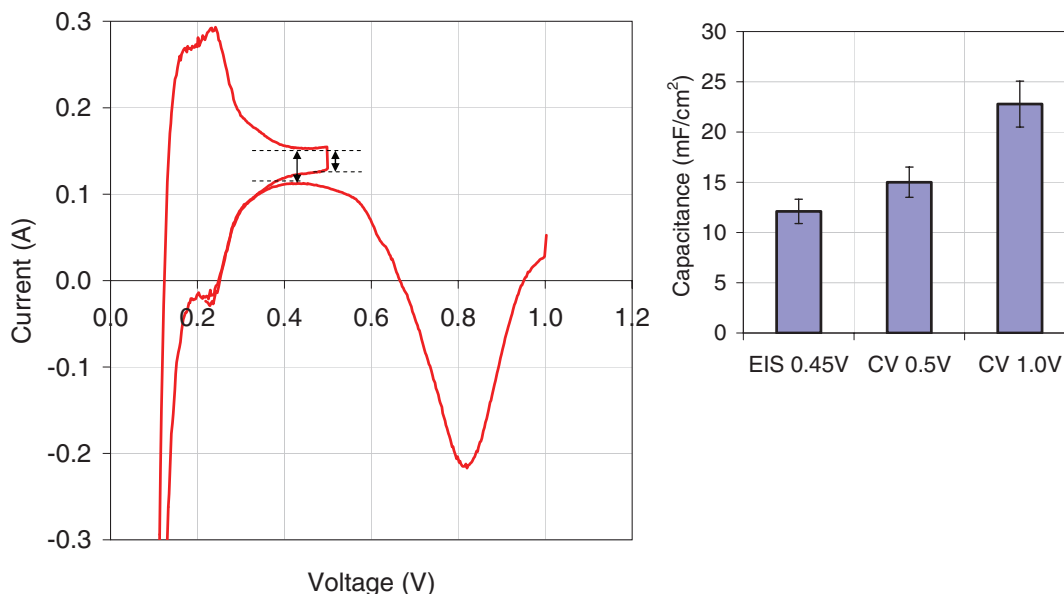
Figure 4. Calculating the Cdl from a CV with and without interference from the Pt oxide desorption peak, and compared to EIS equivalent circuit fit.

may convolute the Cdl measured during CV. As shown in Figure 4, conducting CV below the Pt oxide formation potentials (0.5 V_{RHE}) eliminates this issue and results in a Cdl comparable to EIS analysis. For simplification EIS data was used to calculate the Cdl throughout the remainder of this study.

Figure 1b and 2b shows how the capacitance changed throughout the AST at different UPLs for the cathode CLs using LSAC and MSAC supports, respectively. For UPLs less than or equal to 1.0 V_{RHE} a decrease in the Cdl is observed, which may be associated with the loss of the platinum surface area observed in Figure 1a and 2a. For UPLs > 1.0 V_{RHE} the Cdl initially shows an increase, which is believed to be caused by the generation of hydrophilic oxygenated carbon surface groups from the surface oxidation[11,14,15,16] in Eq. 5. For UPLs > 1.2 V_{RHE} the Cdl initially increases due to the surface oxidation and then decreases due to the loss of carbon surface area from the corrosion of the carbon-oxygen surface groups to CO/CO_2 [Eq. 6]. The LSAC and MSAC MEAs show very similar trends; however, a greater UPL was required to observe a similar change in the LSAC MEA, suggesting it had better corrosion resistance. This is discussed further in the model analysis below.

Semi-Empirical model.— The UPL study was utilized to develop a semi-empirical model that determines the rate constants for the two step carbon corrosion process. Both the initial surface oxidation [Eq. 5] and further corrosion to CO_2 [Eq. 6] were assumed to be first order reactions with respect to the normalized carbon surface area, as described by Equations 7-8.

$$-r_{gr} = -dS_{C,gr}/dt = k_{gr} * S_{C,gr}$$ [7]

$$-r_{ox} = -dS_{C,ox}/dt = k_{ox} * S_{C,ox} - k_{gr} * S_{C,gr}$$ [8]

Where r_{gr} and r_{ox} are the reaction rates ($m^2_{carbon}/m^2_{geometric}$/s) for the graphitic and oxidized surfaces, k_{gr} and k_{ox} are the rate constants (1/s) for the graphitic and oxidized surfaces, and $S_{C,gr}$ and $S_{C,ox}$ are the normalized surface areas ($m^2_{carbon}/m^2_{geometric}$) of the graphitic and oxidized surface respectively.

Previous testing using Pt catalysts of different Pt/C ratios has shown that platinum catalyzes carbon oxidation and corrosion;[6,17,18] however, since this testing used the same Pt/C ratio an assumption of negligible platinum effect was made to simplify the model. Therefore, until improvements to the model are made to account for these phe-

nomena, this model should only be used to compare catalysts with a similar Pt-C interface.

Integrating Equations 7-8 leads to more useful forms of the rate equations described in Eq. 9-10.

$$S_{C,gr} = S_{C,gr}^{o} * exp^{(-kgr*t)}$$ [9]

$$S_{C,ox} = S_{C,gr}^{o} * k_{gr}/(k_{gr} + k_{ox}) * (exp^{(-kgr*t)} - exp^{(-kox*t)})$$ [10]

Where S_{gr}^{o} is the initial graphitic carbon surface area ($m^2_{carbon}/m^2_{geometric}$) and t is the time spent at UPL in seconds.

The initial graphitic carbon surface area was calculated by taking the difference between the total surface area obtained from BET gas adsorption measurements and the catalyst metal surface area measured by CO absorption. This model assumes 1) the entire carbon surface is covered with ionomer and contributes to the Cdl, and 2) the entire surface is initially graphitic; therefore, the initial oxidized carbon surface area was set to zero.

The total Cdl of the carbon was then calculated by multiplying each respective surface area by their specific capacitance as shown in Eq. 11.

$$Cdl_{C,total} = Cdl_{C,gr} * S_{C,gr} + Cdl_{C,ox} * S_{C,ox}$$ [11]

Where $Cdl_{C,total}$ is the total carbon Cdl ($\mu F/cm^2_{geometric}$), $Cdl_{C,gr}$ is the specific capacitance of the graphitized carbon surface ($\mu F/cm^2$), $Cdl_{C,ox}$ is the specific capacitance of the oxidized carbon surface ($\mu F/cm^2$).

Further the total capacitance of the catalyst was calculated in Eq. 12 by adding the capacitance of the platinum surface.

$$Cdl_{total} = Cdl_{C,total} + Cdl_{Pt} * ECSA$$ [12]

Where the Cdl_{Pt} is the specific capacitance of platinum ($\mu F/cm^2$).

The rate constants, k_{ox}, k_{gr}, and specific capacitances, $Cdl_{C,gr}$, $Cdl_{C,ox}$, Cdl_{Pt} were unknowns and were obtained through a successive fitting of the data set shown in Figures 1 and 2. Fitting was accomplished by allowing the fitting parameters to vary in order to minimize the sum of the squared error between model and experiment.

The first parameters to be fit were $Cdl_{C,gr}$ and Cdl_{Pt}, by fitting the total capacitance in the 0.9 and 1.0 V_{RHE} UPL tests, where a negligible surface oxidation and CO_2 corrosion were assumed and any change in Cdl_{total} was solely due to the reduction in ECSA. This assumption depends on the carbon type and may not be valid for non-graphitic carbons, where a lower UPL would be required to make

Table II. Specific capacitance for platinum and graphitic and oxidized carbon surfaces for the LSAC and MSAC catalysts.

Catalyst	C_{gr} Specific Cdl ($\mu F/cm^2$)	C_{ox} Specific Cdl ($\mu F/cm^2$)	Pt Specific Cdl ($\mu F/cm^2$)
LSAC	5.4 +/− 0.2	45	62
MSAC	6.9 +/− 1.1	48	62

this assumption. This resulted in the platinum and graphitized carbon specific capacitances for the LSAC and MSAC catalysts, as listed in Table II. The platinum specific capacitance of 62 $\mu F/cm^2$, determined by taking the slope of ECSA versus Cdl_{total} (Figure 5), was relatively close to the 40 $\mu F/cm^2$ reported in literature.[19,20] This parameter was held constant for all remaining test cases.

Assuming the entire carbon surface was graphitic in all new samples, the $Cdl_{C,gr}$ could be calculated from Eqs. 11-12 based on the beginning of test data. This resulted in an average carbon specific capacitance of 5.4 +/− 0.2 and 6.9 +/− 1.1 $\mu F/cm^2$, for the LSAC and MSAC catalysts, respectively, which was within the 3 to 56 $\mu F/cm^2$ range reported in literature.[15,21,22] These parameters were fixed for the remainder of the analysis.

The rate constants and the specific capacitance of the oxidized carbon surface were fitted using the data set which had the best resolution for the change in Cdl showing both an increase and decrease in Cdl; the 1.3 V_{RHE} for the LSAC catalyst, and the 1.2 V_{RHE} for the MSAC catalyst (shown in Figures 1 and 2). Figure 6 shows the data fit and the change in the graphitized and oxidized surface areas with progressing AST cycles. Since these specific test cases clearly showed the balance between oxidation and corrosion reactions, they were able to give unique solutions for the three stated fitting parameters. The specific capacitance of oxidized carbon ranged from 45 to 48 $\mu F/cm^2$ for both LSAC and MSAC carbons and was assumed to be constant for all other tests, leaving only the two rate constants as fitting parameters.

Figure 6 also shows the correlation between the change in Cdl and the corrosion rate that was calculated directly from the CO/CO_2 in the gas exhaust. This trend exists due to the dependency of Cdl and the corrosion rate on the oxidized carbon surface area modeled here.

With the average values for the specific capacitances fixed, the rate constants were fitted for all UPL tests independently as shown in Figure 7. A clear relationship between the rate constants and the UPL for both carbon supports was observed. The surface oxidation
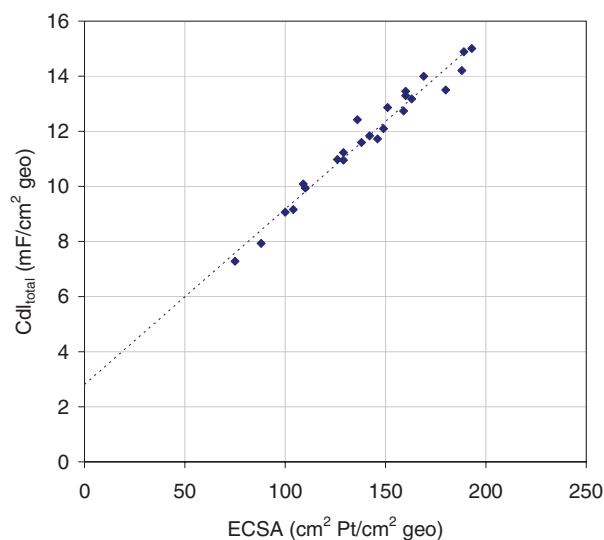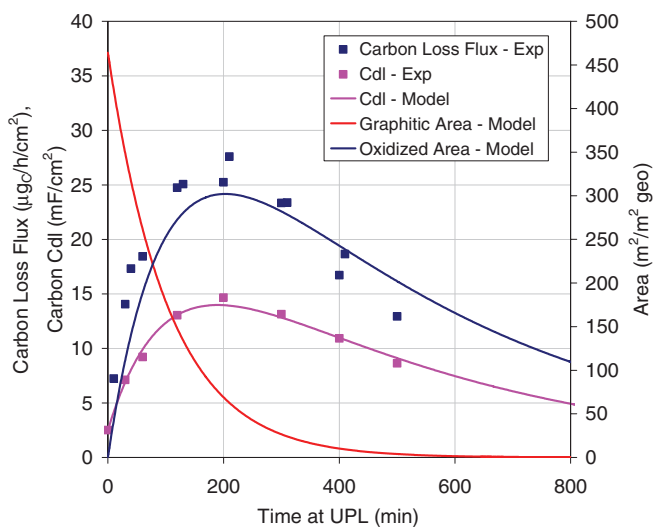
Figure 6. The model fit of the experimental Cdl data as a function of time at UPL. The modeled graphitized and oxidized surface areas are also plotted, highlighting the trend with the corrosion rate measured by the carbon loss in the gas exhaust.

rate constant differed considerably between carbon supports, with the MSAC oxidation rate much faster than the LSAC carbon. It is noted that at higher UPLs the difference in oxidation rates was reduced.

The CO_2 corrosion rate constant was close between carbon supports suggesting the major difference in total corrosion resistance was the first surface oxidation step. Once the surface was oxidized the CO_2 corrosion reaction rate was similar regardless of carbon type.

Effect of UPL dwell time.— Typical start-up/shut-down conditions during fuel cell operation will experience UPLs greater than the open circuit potential for less than one second; therefore, the UPL dwell time between 5 to 600 s was evaluated to understand any differences between transient versus pseudo steady state reaction rate behaviors. Figure 8 shows no trend in the oxidation reaction rate with UPL time and any differences were significantly less than the impact of UPL voltage. The corrosion reaction rate constant did show a slight dependency on dwell time, which was supported by the decreasing trend in carbon loss with increasing dwell time. This agrees with the corrosion current decay, commonly described empirically in literature[23] by the power law $i(t) = kt^{-n}$. While this behavior is consistent for potentiostatic hold tests, it should be noted that there are several factors that could convolute the carbon corrosion response under cycling conditions such as the state of the platinum and carbon surface over time. The Pt particle size and oxide coverage will vary with UPL time as will the amount of water and oxide groups at the carbon surface.

Effect of temperature and gas RH.— A temperature and gas RH sensitivity study utilizing the LSAC catalyst is shown in Figure 9. A 1.4 V_{RHE} UPL was used to obtain a faster corrosion response enabling shorter test duration and an UPL dwell time of ten minutes was used to reduce the total cycle number and minimize the platinum dissolution effects.

At a 1.4 V_{RHE} UPL the oxidation rate constant shows greater response to both temperature and gas RH, with significantly greater rates at high temperature and RH compared to the corrosion rate constant. In an effort to best normalize the effect of gas RH, shown in the Arrhenius plot in Figure 10, the rate constants were divided by the water content of the ionomer, which required the use of an empirical relationship between gas RH and Nafion water content.[24] This also required adding exponential factors on the Nafion water content parameter of 0.9 and 0.15 for the oxidation and corrosion reactions, respectively. While the motivation for this normalization

Figure 5. The slope of Cdl_{total} versus ECSA reveals the specific capacitance of Pt to be 62 $\mu F/cm^2$. The y-intercept, representing the total carbon capacitance of a new cathode CL, was used to calculate the specific capacitance of both LSAC and MSAC supports shown in Table II.
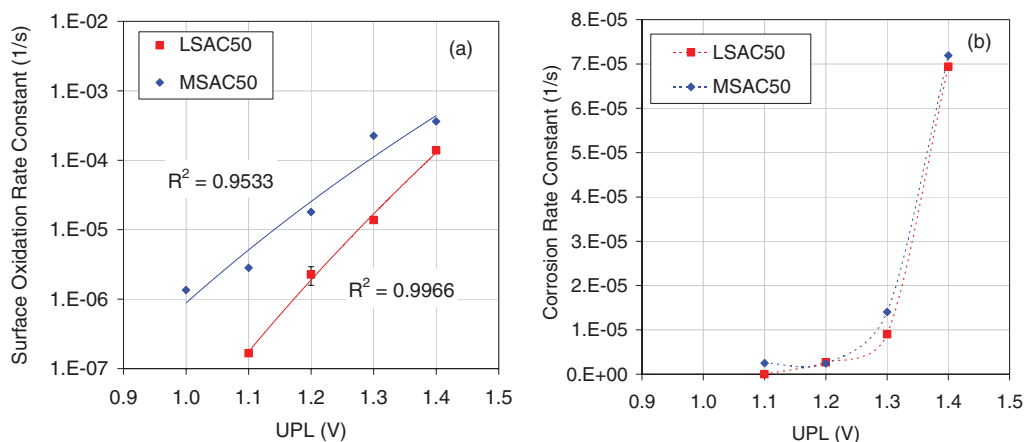
Figure 7. The fitted rate constants for the LSAC50 and MSAC50 carbon supports as a function of AST UPL for the (a) surface oxidation, and (b) CO_2 corrosion reactions.
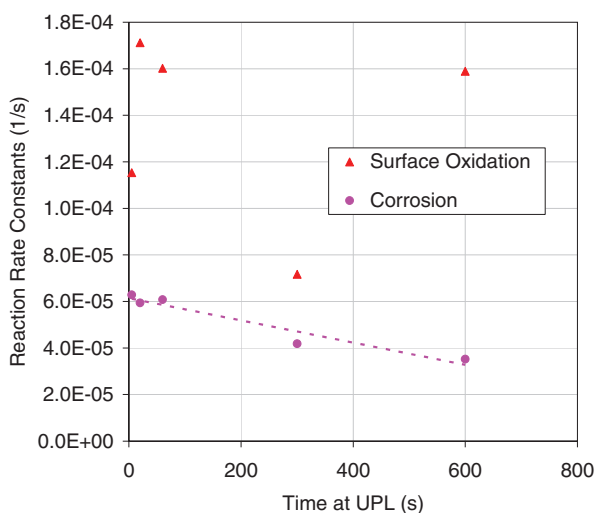

Figure 8. The fitted oxidation and corrosion rate constants for the LSAC carbon at varying UPL dwell times.

Table III. Arrhenius activation energy and prefactor for the LSAC catalyst oxidation and corrosion reaction rates.

Arrhenius Parameters	Arrhenius Pre-Factor (s-1)	Activation Energy (kJ/mol)
Oxidation Rate	2.95E + 09	90.6
Corrosion Rate	7.37E + 07	82.6

was to enable a simple way of modeling both temperature and gas RH effects, the exponential factors may give further information on the relationship of the oxidation and corrosion reactions with water, such as a possible stoichiometry effect. More work is required to explore this further.

Arrhenius parameters, including activation energy, were calculated before the normalization for water content and are shown in Table III. These values are comparable to the 106 +/− 17 kJ/mol quoted for the thermal combustion of carbon from a Pt/C catalyst.[17]

A validation of the model was conducted using the temperature study as shown in Figure 11, which compares the measured loss of carbon to the modeled loss of carbon surface area, on a percentage basis. It is assumed the percent mass loss and surface area loss are equivalent. The agreement between model and data is reasonable with
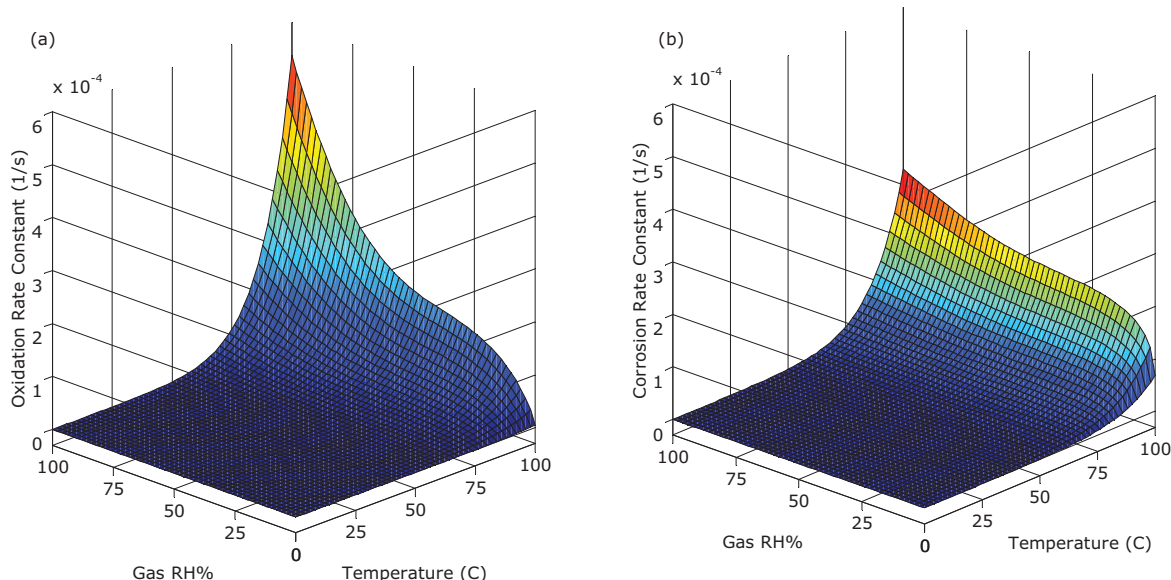

Figure 9. The reaction rate constants as a function of temperature and gas RH for the (a) carbon oxidation reaction, and (b) the carbon corrosion reaction.
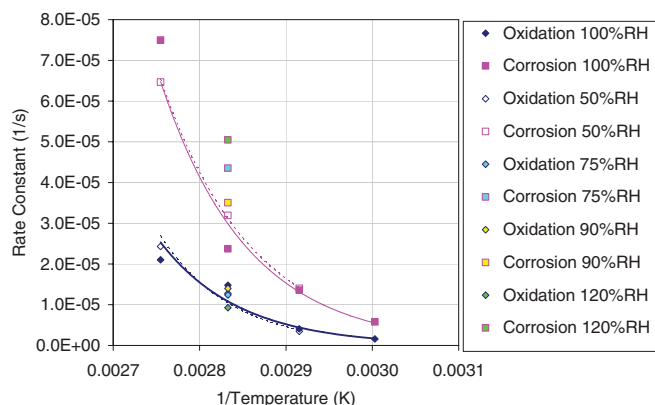
Figure 10. Arrhenius plot after normalizing for Nafion water content based on the gas RH.

Figure 12. Voltage loss as a function of carbon loss as measured by CO/CO_2 in the cathode gas exhaust. Cell voltage was measured at 1.0 A/cm^2, 75°C, 5 psig.

greater differences occurring at lower temperatures. The discrepancy between model and experiment can be speculated to be mainly caused by the simplifying model assumptions. As partially discussed above the model assumptions consist of the following: the corrosion reactions are modeled as two first order reactions, the platinum interaction is consistent and similar between all tests, both catalysts tested started with a fully graphitic surface, and finally there was no surface renewal. This last assumption suggests that all surface area is available at beginning of test and once that surface has reacted it is lost. In reality, as carbon corrodes to CO_2 a graphitic surface will remain to be oxidized again. This process will repeat until the carbon agglomerates shrink, eventually causing the CL structure to collapse, eventually breaking electrical percolation. Modeling this would require a more fundamental approach possibly using a combined shrinking particle/shrinking core model.[25]

The current model will have limited applicability for detailed understanding of the carbon corrosion process beyond the two step model described, including other intermediate reactions modeled in detail elsewhere,[26] and the response from different catalyst structures. Further additions will be required to expand model capability. The advan-

tage of this simple model is its ability to predict the Cdl response over the range of conditions described above, which has been correlated to performance loss.

Using model to predict onset of performance loss.— For the Pt catalyst supported on LSAC the onset of performance loss translated to a 20–40% carbon loss, as measured by the amount of CO and CO_2 in the cathode and anode gas exhaust and shown in Figure 12. During the initial stages of degradation where surface oxidation is dominant there is a 5–15 mV performance improvement. Although not discussed in detail here, this performance gain has been correlated to an increase in the CL proton conductivity, which has been hypothesized to be caused by the hydrophilic nature of the oxidized surface and the possible interaction with ionomer.

As the carbon support was fully corroded to CO_2 the CL collapsed forming a condensed layer with lower porosity, resulting in performance loss due to the introduction of oxygen mass transport
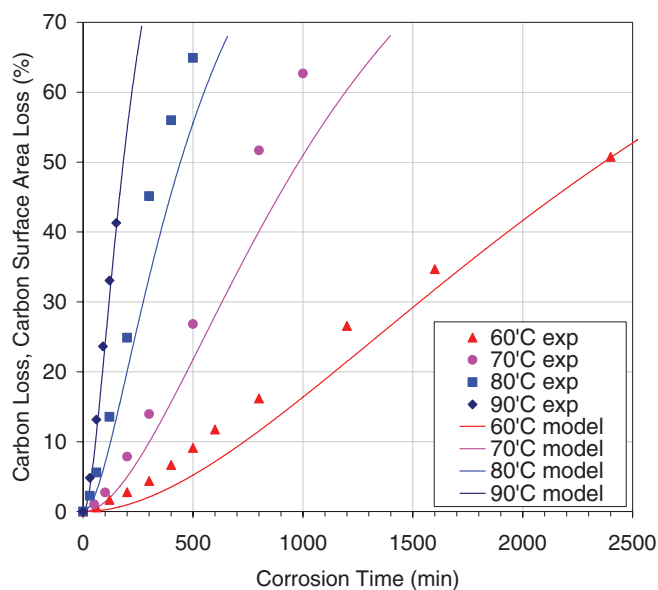

Figure 11. Model validation based on the prediction of the percent loss of carbon surface area versus the percent loss of carbon as measured in the gas exhaust. Symbols represent the experimental data and the lines represent the model prediction.
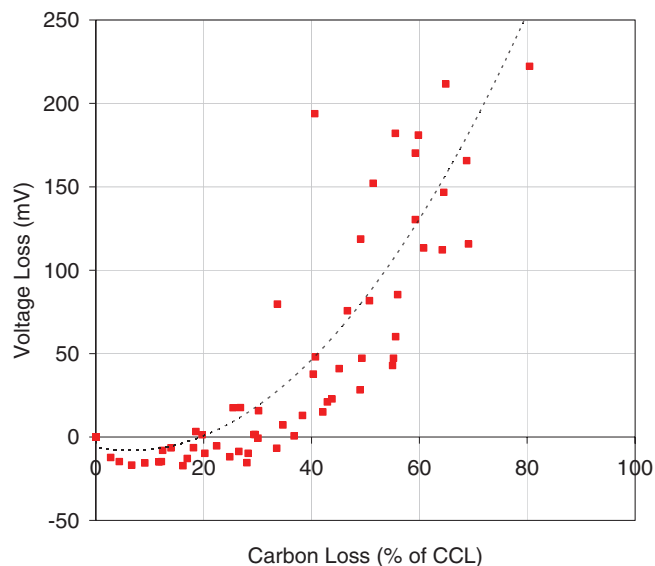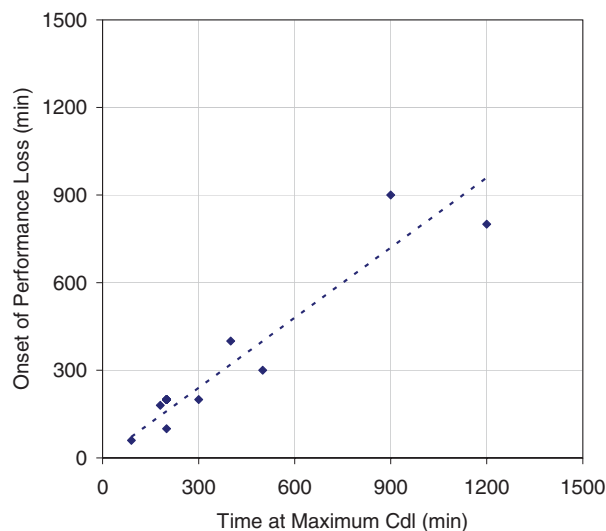

Figure 13. Correlation between the maximum double layer capacitance to the onset of cell voltage performance loss due to carbon support corrosion. Cell voltage was measured at 1.0 A/cm^2, 75°C, 5psig.

limitations. The porosity was calculated based on a mass balance, utilizing the measured carbon loss and CL thickness obtained by SEM. For the LSAC, the onset of performance loss occurred within a porosity range of 55–60%.

The model presented is capable of predicting the Cdl response over a specified range of UPL, temperature, and gas RH. To make this model more useful a correlation between the Cdl and performance loss is presented in Figure 13, which plots the time at the maximum Cdl versus the onset of performance loss. It is clear that the onset of performance loss occurs at or just before the maximum Cdl is reached. Utilizing this correlation enables one to use this model to predict the onset of performance over a range of UPL, temperature, and gas RH.

Conclusions

A semi-empirical model was developed to describe the two steps in the carbon support corrosion mechanism. The specific capacitances for platinum, graphitized carbon, and oxidized carbon were determined and found to be within expected values reported in literature.

Comparing two different carbons showed a significant difference in the rate constant of the first surface oxidation step while the rate constant of the CO_2 corrosion step was similar between carbons, suggesting the initial oxidation reaction was the limiting step for corrosion resistance.

As expected the reaction rates for both steps increased with increasing UPL, temperature, and gas RH, with the oxidation reaction having a greater dependence on all three variables. Normalization of the gas RH was done in order to simplify the relationships between the reaction rates and temperature and gas RH. The exponential factor required to do this effectively, suggests there may be a stoichiometry dependence of water in both the oxidation and corrosion reactions.

The addition of the Cdl/performance loss correlation to this semi-empirical model allows one to predict the onset of performance loss due to carbon support corrosion as a function of UPL, temperature, and gas RH.

Acknowledgments

References

1. K. Kinoshita, *Carbon: Electrochemical and Physiochemical Properties*, p. 316, John Wiley & Sons, New York (1998).
2. W. Bi, G. E. Gray, and T. F. Fuller, *Electrochemical and Solid-State Letters*, **10**, B101 (2007).
3. X. Yu and S. Ye, *J. Power Sources*, **172**, 145 (2007).
4. M. V. Lauritzen, P. He, A. P. Young, S. Knights, V. Colbow, and P. Beattie, *J. New Mat. Electrochem. Systems*, **10**, 143 (2007).
5. USCAR Fuel Cell Tech Team Cell Component Accelerated Stress Test Protocols for PEMFCs, http://www1.eere.energy.gov/hydrogenandfuelcells/pdfs/component_durability_may_2010.pdf10.1149/2.061304jes.html.
6. E. Passalacqua, P. L. Antonucci, M. Vivaldi, A. Patti, V. Antonucci, N. Giordano, and K. Kinoshita, *Electrochimica Acta*, **37**, 2725 (1992).
7. S. Maass, F. Finsterwalder, G. Frank, R. Hartmann, and C. Merten, *J. Power Sources*, **176**, 444 (2008).
8. D. A. Stevens, M. T. Hicks, G. M. Haugen, and J. R. Dahn, *J. Electrochem. Soc.*, **152**, A2309 (2005).
9. T. R. Ralph, G. A. Hards, J. E. Keating, S. A. Campbell, D. P. Wilkinson, M. Davis, J. St-Pierre, and M. C. Johnson, *J. Electrochem. Soc.*, **144**, 3845 (1997).
10. E. B. Easton and P. G. Pickup, *Electrochimica Acta*, **50**, 2469 (2005).
11. A. Young, J. Stumper, and E. Gyenge, *J. Electrochem. Soc.*, **156**, B913 (2009).
12. M. Matsumoto, T. Miyazaki, and H. Imai, *J. Phys. Chem. C*, **115**, 11163 (2011).
13. A. Kongkanand and J. M. Ziegelbauer, *J. Phys. Chem. C*, **116**, 3684 (2012).
14. K. H. Kangasniemi, D. A. Condit, and T. D. Jarvi, *J. Electrochem. Soc.*, **151**, E125 (2004).
15. M. J. Bleda-Martinez, J. A. Macia-Agullo, D. Lozano-Castello, E. Morallon, D. Cazorla-Amoros, and A. Linares-Solano, *Carbon*, **43**, 2677 (2005).
16. C. H. Paik, G. S. Saloka, and G. W. Graham, *Electrochemical and Solid-State Letters*, **10**, B39 (2007).
17. D. A. Stevens and J. R. Dahn, *Carbon*, **43**, 179 (2005).
18. N. Linse, L. Gubler, G. G. Scherer, and A. Wokaun, *Electrochimica Acta*, **56**, 7541 (2011).
19. M. Breiter, *J. Electroanal. Chem.*, **7**, 38 (1964).
20. A. Parthasarathy, B. Dave, S. Srinivasan, J. A. Appleby, and C. R. Martin, *J. Electrochem. Soc.*, **139**, 1634 (1992).
21. K. Kinoshita, *Carbon: Electrochemical and Physiochemical Properties*, p. 294, John Wiley & Sons, New York (1998).
22. T. A. Centeno and F. Stoeckli, *Electrochimica Acta*, **52**, 560 (2005).
23. P. Serp and J. L. Figueiredo, *Carbon Materials for Catalysis*, p. 465, John Wiley & Sons, New York (2009).
24. T. E. Springer, T. A. Zawodzinski, and S. Gottesfeld, *J. Electrochem. Soc.*, **138**, 2334 (1991).
25. S. Homma, S. Ogata, J. Koga, and S. Matsumoto, *Chemical Eng. Science*, **60**, 4971 (2005).
26. K. G. Gallagher and T. F. Fuller, *Phys. Chem. Chem. Phys.*, **11**, 11557 (2009).